Ultrasound-driven fabrication of high-entropy alloy nanocatalysts promoted by alcoholic ionic liquids

Francis Okejiri, Zhenzhen Yang*, Hao Chen, Chi-Linh Do-Thanh, Tao Wang, Shize Yang*, and Sheng Dai*

The University of Tennessee, USA.
Oak Ridge National Laboratory, USA.
Eyring Materials Center, Arizona State University, USA

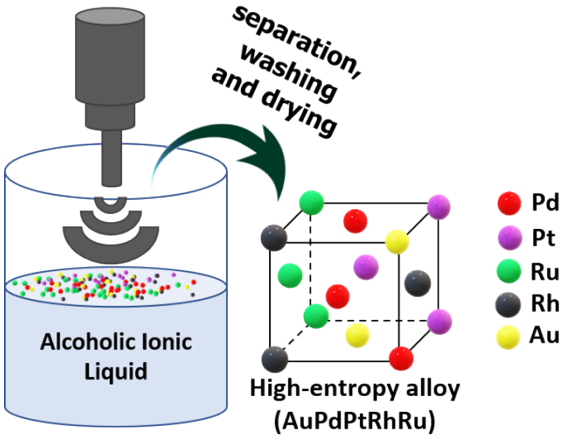

A facile synthesis of high-entropy alloy nanocatalysts was realized via an ultrasound-driven wet chemistry method promoted by an alcoholic ionic liquid.

Nano Research

ISSN 1998-0124 CN 11-5974/O4
https://doi.org/(automatically inserted by the publisher)

Research Article

Ultrasound-driven fabrication of high-entropy alloy nanocatalysts promoted by alcoholic ionic liquids

Francis Okejiri[1,2], Zhenzhen Yang[2] (✉), Hao Chen[1], Chi-Linh Do-Thanh[1], Tao Wang[2], Shize Yang[3,†] (✉), Sheng Dai[1,2] (✉)

[1] *Department of Chemistry, The University of Tennessee, Knoxville, TN 37996, USA*
[2] *Chemical Sciences Division, Oak Ridge National Laboratory, Oak Ridge, TN 37831, USA*
[3] *Center for Functional Nanomaterials, Brookhaven National Laboratory, Upton, New York 11973, USA*
[†] *Eyring Materials Center, Arizona State University, Tempe, AZ 85287, USA*

Received: day month year / **Revised:** day month year / **Accepted:** day month year (automatically inserted by the publisher)

ABSTRACT

High-entropy alloy nanoparticles (HEA-NPs) are highly underutilized in heterogeneous catalysis due to the absence of a reliable, sustainable, and facile synthetic method. Herein, we report a facile synthesis of HEA nanocatalysts realized via an ultrasound-driven wet chemistry method promoted by alcoholic ionic liquids (AILs). Owing to the intrinsic reducing ability of the hydroxyl group, AILs were synthesized and utilized as environmentally friendly alternatives to conventional reducing agents and volatile organic solvents in the synthetic process. Under high-intensity ultrasound irradiation, Au^{3+}, Pd^{2+}, Pt^{2+}, Rh^{3+}, and Ru^{3+} ions were co-reduced and transformed into single-phase HEA (AuPdPtRhRu) nanocrystals without calcination. Characterization results revealed that the as-synthesized nanocrystals are composed of elements of Au, Pd, Pt, Rh, and Ru as expected. Compared to the monometallic counterparts such as Pd-NPs, the carbon-supported HEA nanocatalysts showed superior catalytic performance for selective hydrogenation of phenol to cyclohexanone in terms of yield and selectivity. Our synthetic strategy provides an improved and facile methodology for the sustainable synthesis of multicomponent alloys for catalysis and other applications.

KEYWORDS

High-entropy alloy, alcoholic ionic liquid, sustainability, ultrasonication, nanoparticles, hydrogenation

1 Introduction

High-entropy alloys (HEAs) are a unique class of materials with great technological prospects. Unlike traditional alloys, which do not exceed three elements, HEAs are based on the premise of integrating near-equimolar concentrations of five or more elements to form a single-phase solid solution [1, 2]. Nanosized HEAs are highly underutilized in heterogeneous catalysis due to the absence of a reliable, sustainable, and facile synthetic method and may constitute a whole new paradigm in catalysis [3-8]. There has been a growing interest in the development of simple processes to fabricate HEA nanocatalysts for thermally-driven and electrocatalytic reactions (Table S1) [2, 9-21]. Hu and coworkers have reported a carbothermal shock method in which metal salt precursors loaded onto carbon-nanofibers were thermally shocked to obtain HEA-nanoparticle (NP) catalysts [9]. However, this synthetic strategy is limited to the production of NPs immobilized on conductive oxygenated carbon supports. Immobilization of ultrasmall-sized HEA-NPs on granular supports has been realized by the fast-moving bed pyrolysis method following wet impregnation [22]. The drawback to this fabrication strategy is that it is technologically demanding and requires highly specialized equipment to rapidly raise the temperature of the mixed metal precursors to 923 K in less than 5 seconds. Nanoporous HEAs with enhanced surface area and uniform pore structure have been synthesized via the dealloying method [23, 24]. While the scalability of this remarkable strategy is highly promising, the inevitable microstructural coarsening resulting from the high-temperature treatment (> 1123 K) degrades the functionality of the materials over time. Also, HEA-NP-graphene composite has been synthesized by mechanical alloying of the pure metal powders with graphite, followed by sonication-based exfoliation [25]. The distribution in the composition between the NPs is unsuitably large [25]. More recently, Chen et al. synthesized monodispersed HEA-NPs by converting a two-phase core@shell NPs to single-phase HEA-NPs via annealing [10]. Other promising strategies that have been reported include sputtering deposition [26], kinetically controlled laser synthesis [16], solvothermal synthesis [27], being limited by the ultrahigh vacuum requirement, restrictive element applicability, and low productivity, respectively.

Studies have shown that liquids irradiated with high-intensity ultrasound generate acoustic cavitation, which drives bubble formation, growth, and implosive collapse in a monetary

Address correspondence to Sheng Dai, dais@ornl.gov; Zhenzhen Yang, yangz3@ornl.gov; Shize Yang, syang212@asu.edu

lifespan while producing enormous heat and pressure in a highly localized region (hotspot) [28]. This transient localized hotspot with a temperature above 5000 K and pressures exceeding 1000 atm can drive a high-energy chemical reaction and serve as an exceptional route for nanoparticle synthesis [29, 30]. Taking advantage of this unique phenomenon, we recently demonstrated the feasibility of fabricating HEA-NPs via an ultrasound-driven wet chemistry method using ethylene glycol (EG) as the reaction medium [31]. Unfortunately, the resultant NPs displayed a two-phase microstructure, requiring further heat treatment at 700 ºC under N_2 to be transformed into single-phase HEA nanocrystals. A single-step ultrasound-driven pathway will rely on the design of multifunctional reaction media capable of well dissolving and reducing the metal species while simultaneously stabilizing the as-afforded HEA NPs. Room-temperature ionic liquids (ILs) can be tailored to meet these requirements due to the relative ease at which simple and small alterations can be made to their chemical structure[32-37].

Rationally, owing to the intrinsic reducing ability of the hydroxyl group, alcohol-functionalized ionic (AILs) was fabricated as the desired multifunctional reaction media in the present study. Under high-intensity ultrasound irradiation, Au^{3+}, Pd^{2+}, Pt^{2+}, Rh^{3+}, and Ru^{3+} ions were co-reduced by the AIL and transformed into single-phase HEA (AuPdPtRhRu) nanocrystals, effectively eliminating the need for an external heat-treatment process. Notably, the hydroxyl functionality played a significant role in the formation of single-phase nanocrystals of AuPdPtRhRu in one step. Characterization results revealed that the as-obtained nanocrystals are composed of elements of Au, Pd, Pt, Rh, and Ru as expected. Compared to the monometallic counterparts such as Pd-NPs, the carbon-supported HEA-NP catalysts showed superior catalytic performance for selective hydrogenation of phenol to cyclohexanone in terms of yield and selectivity. This synthetic strategy provides an improved and facile methodology for the sustainable synthesis of multicomponent alloys in one step under mild conditions.

2 Experimental

2.1 Synthesis of the ionic liquid - [HEMMor][NTf_2]

N-(2-hydroxyethyl)-N-methylmorpholinium bis(trifluoromethylsulfonyl)imide) abbreviated as [HEMMor][NTf_2] was synthesized according to previous reports with some modifications [39]. N-methylmorpholine (0.55 mol) and excess 2-bromoethanol (0.60 mol) were mixed with 300 mL acetonitrile in a round-bottom flask and stirred at 90 °C for 12 h under an N_2 atmosphere. The solvent was removed under reduced pressure, and the residue was washed with ethyl ether to obtain N-(2-hydroxyethyl)-N-methylmorpholinium bromide ([HEMMor][Br]) as a crystalline solid. The solid was redissolved in 300 mL deionized water (DI) and decolorized with activated charcoal by refluxing at 70 °C overnight. The aqueous layer was recovered via vacuum filtration and used for the anionic exchange with lithium bis(trifluoromethylsulfonyl)imide (0.55 mol) at room temperature. The non-aqueous layer was extracted in ethyl acetate and dried under removed pressure to obtain HEMMor][NTf_2] as a clear, viscous liquid. Other ILs (Scheme 1) utilized in this work, including ethyl-N-methylmorpholinium bis(trifluoromethylsulfonyl)imide ([EMMor][NTf_2]) and N-(2-hydroxyethyl)-N-methylmorpholinium tetrafluoroborate ([HEMMor][BF_4]), were synthesized in a similar manner as described in the Electronic Supplementary Material (ESM) and characterized by NMR spectroscopy (Fig. S1 – S2).

2.2 Synthesis of HEA-NPs/C (AuPdPtRhRh-NPs/C)

An aqueous solution of the metal precursors was made by the dissolution of 0.005 mmol each of $HAuCl_4{\cdot}3H_2O$, K_2PdCl_4, K_2PtCl_4, $RhCl_3$, and $RuCl_3$ in 5 mL DI water. The precursors were combined with a calculated mass of XC-72 carbon support pre-dispersed in a 30 mL IL for a total metallic loading of 10 wt.%. The mixture was exposed to sonication treatment for 10 min by direct immersion of ultrasonic titanic horn operating at 20 kHz at ambient conditions, as shown schematically in Fig. 1. When the sonication time was reached, the solid was recovered by centrifugation and washed thoroughly with DI before being dried in an oven at 100 °C overnight. The monometallic counterparts, including Au-NPs/C and Pd-NPs/C, were synthesized in a similar manner using the corresponding metal precursor.

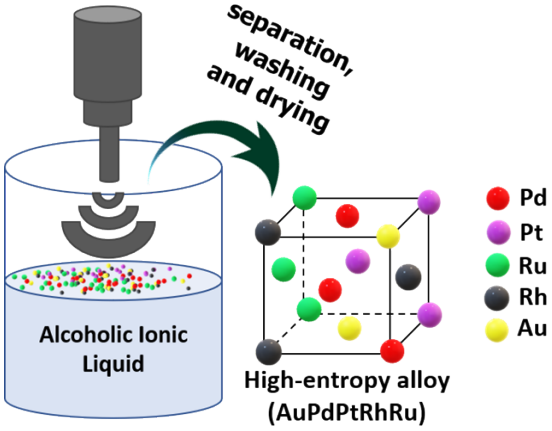

Figure 1 Schematic illustration of the synthesis of high-entropy alloy nanocatalysts realized via an ultrasound-driven wet chemistry method promoted by an alcoholic ionic liquid.

2.3 Characterization of HEMMor][NTf_2]

Proton nuclear magnetic resonance (^{1}H NMR) spectra were recorded on JEOL JNM-ECZS 400 MHz spectrometer using dry DMSO-d_6 as the solvent. The chemical shifts are in ppm. The splitting patterns are represented by the following abbreviations: s (singlet), d (doublet), t (triplet), q (quartet), and m (multiplet).

2.4 Characterization of HEA-NPs/C (AuPdPtRhRh-NPs/C)

X-ray diffraction (XRD) patterns were recorded on a PANalytical Empyrean diffractometer with Cu Kα1 radiation (λ = 1.5406 Å), operated at 45 kV and 40 mA. The 2θ range angles were scanned between 20 to 80° at a step size of 0.02 °. High-angle annular dark-field scanning transmission electron microscopy (HAADF-STEM) images and energy-dispersive X-ray (EDS) spectra were collected on FEI Talos F200X microscope operated at 200 keV. The particle size distribution was estimated by randomly measuring more than 200 particles on the images. The elemental composition was determined by

inductively coupled plasma optical emission spectroscopy (ICP-OES) analysis performed on Agilent 5110 ICP-OES spectrometer. The sample was dissolved in aqua regia and diluted with 2.0 % nitric acid prior to analysis.

2.5 Hydrogenation of phenol

Phenol hydrogenation was performed in a 100 mL stainless steel autoclave equipped with a pressure gauge and a magnetically driven stir bar. In a typical run, 1.3 mmol of phenol, catalyst (2.8 mol% relative to phenol), and 6.0 mL hexane were loaded into the reactor and sealed properly.

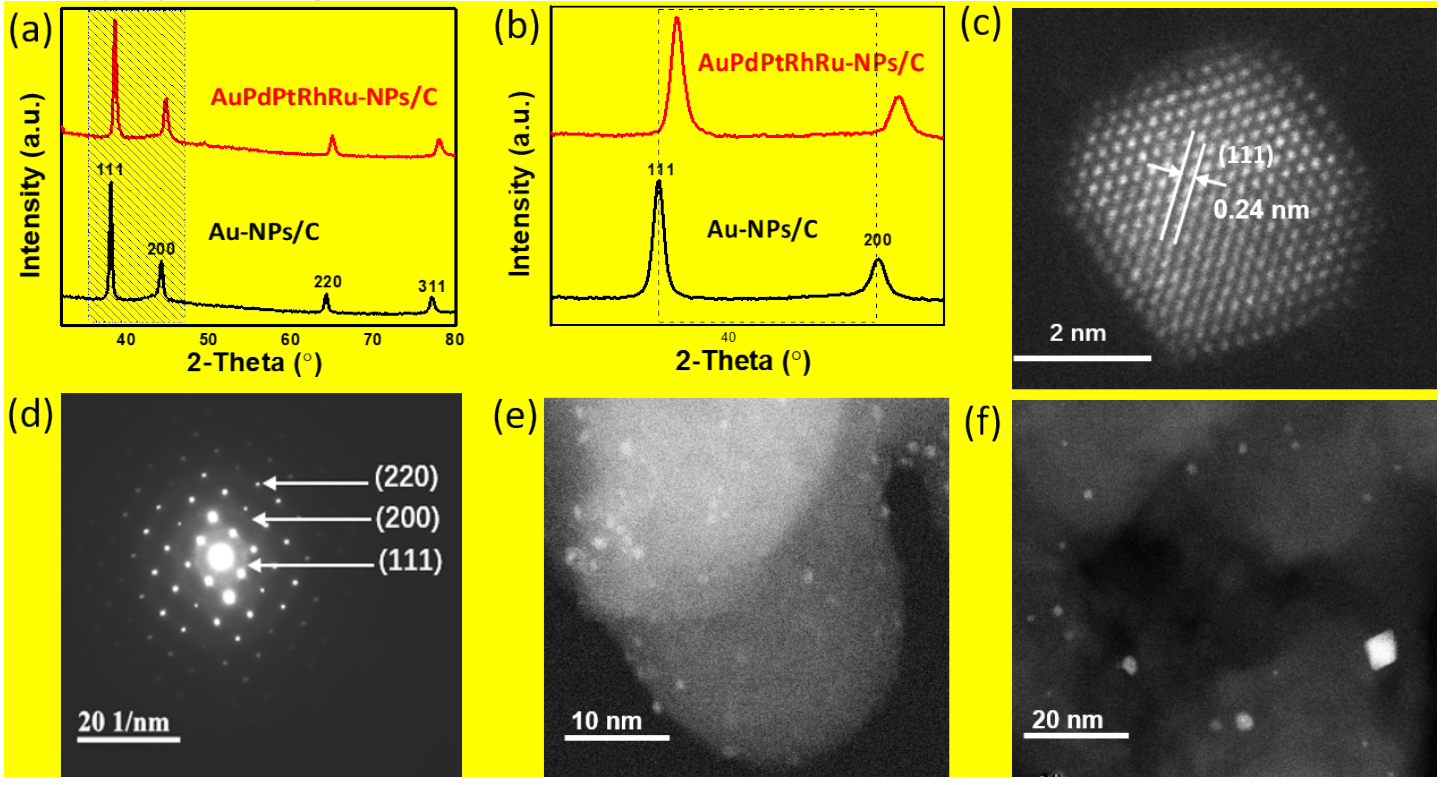

Figure 2 (a) XRD patterns of the supported high-entropy alloy nanocatalysts (AuPdPtRhRu-NPs/C) and the gold standard (Au-NPs/C). The shift in reflection positions of AuPdPtRhRu-NPs/C relative to Au-NPs/C is denoted by the dotted lines in (b). (c) HR-STEM image of AuPdPtRhRu-NPs/C (HEA-NPs/NC) showing a lattice fringe spacing of 0.24 nm consistent with (111) plane of a face-centered cubic crystal structure. (d) SAED pattern of HEA-NPs/C displaying a Debye-Scherrer ring pattern consistent with a polycrystalline fcc lattice. (e) STEM image of HEA-NPs/C at a higher resolution. (f) STEM image of HEA-NPs/C at a lower resolution.

The residual air was expelled from the reactor by purging with purified hydrogen five times before being pressurized to the desired pressure. The reactor was heated in an oil bath at 150 °C with constant stirring for a predetermined period. At the end of the reaction time, the reactor was cooled to room temperature and depressurized. The catalysts were recovered by centrifugation, and the supernatant liquid analyzed using a gas chromatograph (Agilent 9790-GC) equipped with a flame ionization detector (FID).

3 Results and discussion

3.1 Synthesis and characterization of HEA-NPs/C

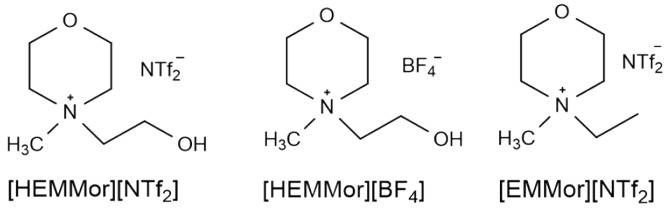

Scheme 1 Structures of the ionic liquids used in this work.

First, the AIL ([HEMMor][NTf_2]) was synthesized via a two-step process and characterized by NMR spectroscopy (Fig. S3). To test the feasibility of fabricating supported HEA nanocatalysts by our ultrasound-driven AIL-promoted strategy, commercial XC-72 carbon support, and the metal salt precursors were dispersed in the AIL and exposed to high-intensity ultrasound irradiation for 10 mins. The product was recovered by centrifugation, washed in DI water, and characterized by XRD, STEM, EDS, and ICP-OES. For simplicity, the as-obtained carbon-supported HEA-NP catalyst is denoted as HEA-NPs/C.

The crystallinity of HEA-NPs/C was determined by the XRD technique and presented in Fig. 2 (a). HEA-NPs/C showed four distinct peaks that correspond to the standard Braggs reflections ((111), (200), (220), and (311)) of face-centered cubic (fcc) lattice with a preferential growth along the (111) plane. The shift in characteristic reflection with respect to Au-NPs/C standard, shown in Fig. 2 (b), is attributed to the change in lattice parameters. The absence of secondary diffraction peaks suggests that Pt, Pd, Rh, and Ru particles are well incorporated into the Au lattice to form an entropy-stabilized single-phase solid solution.

The high-resolution (HR)-STEM image in Fig. 2 (c) and S4

show lattice fringe spacing of 0.24 nm, which is consistent with the (111) plane of a fcc crystal lattice; the corresponding selected area electron diffraction (SAED) pattern additional corroborates this. The radial intensity line profile as a function of reciprocal lattice distance extracted from the SAED pattern is presented in Fig. 2 (d).

Figures 2 (e) and (f) display the STEM image of HEA-NPs/C showing nanocrystalline particles of AuPdPtRhRu dispersed on the XC-72 carbon support. The particle size range is narrow which may have resulted from the controllable growth of NPs induced by the electrostatic and steric properties of the IL. There are, however, quite a few remarkably larger particles that possibly resulted from inhomogeneous mixing of the precursor ions and their subsequent sintering during the sonication process. Overall, the majority of the particles have diameters in the nanoscale range.

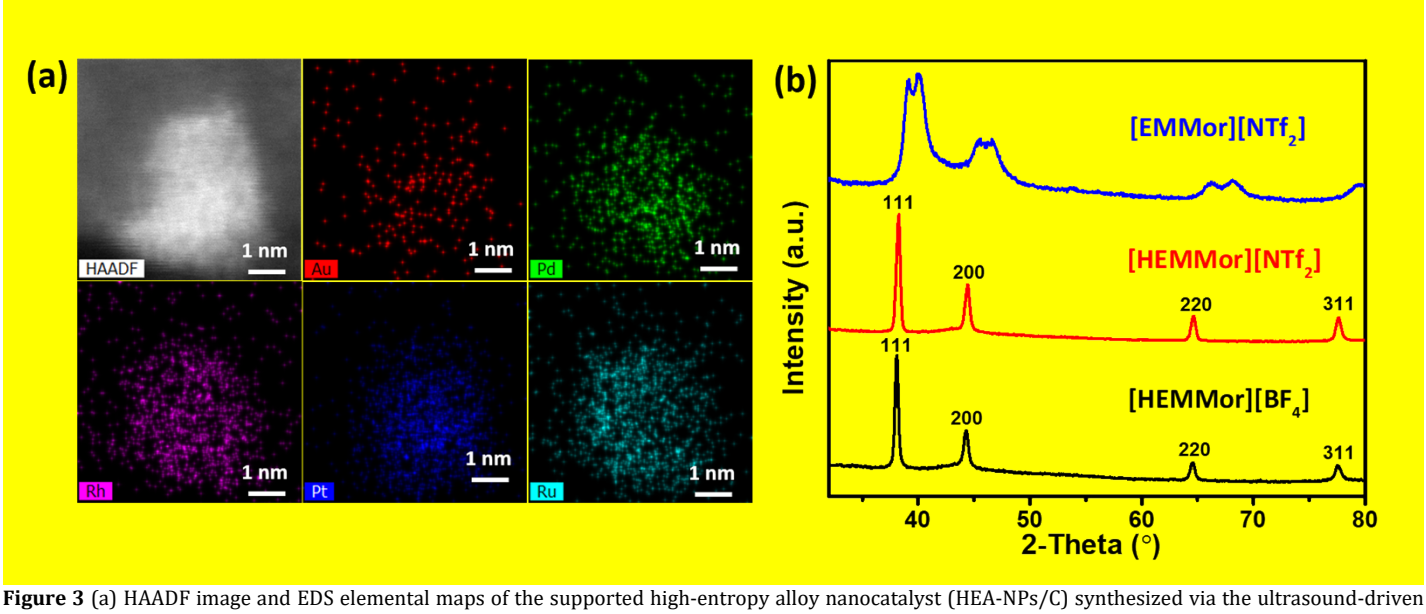

Figure 3 (a) HAADF image and EDS elemental maps of the supported high-entropy alloy nanocatalyst (HEA-NPs/C) synthesized via the ultrasound-driven wet chemistry method promoted by alcoholic ionic liquid (AIL). (b) XRD patterns of multicomponent alloys derived in different kinds of IL: (AIL - bottom two and non-AIL - top one).

Figure 3 (a) shows the STEM-EDS elemental map of HEA-NPs/C.

The uniform distribution of Au, Pd, Pt, Rh, and Ru in the nanosphere directly validates the formation of an alloy system. The EDS spectrum in Fig. S6 shows the signal intensities of all five metals, which additionally corroborates this. The EDS elemental map analyses of different areas on the sample were acquired (Fig. S7) to demonstrate the homogeneity of HEA-NPs/C. The results show that HEA-NPs/C is both structurally and chemically homogeneous.

The elemental composition of HEA-NPs/C was further determined by the ICP-OES analysis. The atomic percent of Au, Pd, Pt, Rh, and Ru, are respectively 19.8, 19.0, 20.5, 21.3, and 19.4, which approximates to 1:1:1:1:1 mole ratio used in the starting materials. Also, the overall metal loading was determined to be 9.7 wt.%, which is close to the theoretical 10 wt.% metal loadings. We can conclude from these results that a single-phase solid solution of AuPdPtRhRh-NPs has been realized in one step via the proposed ultrasound-driven wet chemistry protocol promoted by AIL.

To demonstrate the flexibility of our synthetic strategy, binary, ternary, and quaternary multicomponent alloys were fabricated following the synthetic protocol. As seen in Figure S8, the XRD patterns, like the quinary alloy (Figure 2a) displayed four distinct peaks that correspond to the standard Braggs reflections of the fcc crystal lattice with no phase segregation. Also, a quinary alloy with theoretical atomic percent of 15, 25, 25, 20, and 15 for Au, Pd, Pt, Rh, and Ru respectively was synthesized to investigate how easily the alloy composition can be controlled. The actual atomic percent based on the ICP-OES data analysis was 14.7, 24.9, 25.2, 19.8, and 15.4 which corresponds to approximately 0.6:1:1:0.8:0.6 mole ratio respectively as expected. Additionally, we utilized [HEMMor][BF_4], which has markedly distinct physical properties from [HEMMor][NTf_2] as the reaction medium to demonstrate the flexibility of the reaction medium. The as-obtained nanocrystals, as seen in Fig. 3 (b), showed similar diffraction peaks as those from [HEMMor][NTf_2], which unambiguously proved the adaptability of our synthetic protocol.

To underscore the importance of the hydroxyl functionality in the formation of single-phase nanocrystals of AuPdPtRhRh in one step, [HEMMor][NTf_2] was replaced with the "non-hydroxyl" counterpart, i.e. [EMMor][NTf_2] as the reaction medium. The formation of phase-segregated XRD patterns displayed in Fig. 3 (b) provides evidence that the hydroxyl functionality is crucial in the formation of single-phase HEA nanocrystals in one step.

3.2 Catalytic performance of HEA-NPs/C towards selective hydrogenation of phenol

Cyclohexanone is an important chemical intermediate in the manufacture of ε-caprolactam, a raw material used in the production of nylon-6 [38-40]. It can be obtained by the

oxidation of cyclohexane which requires high temperature and pressure and often leads to the formation of undesirable side products [41]. Selective hydrogenation of phenol (Scheme 2) is an alternative pathway in which cyclohexanone selectivity largely depends on the properties of the catalysts [41-49]. Tunning the electronic and geometric structures of the catalysts is a workable strategy to improve performance, as has been demonstrated from the results of various bimetallic catalysts [50-55]. HEAs consist of even more elements and thus regulate the geometric and electronic structures to a larger extent. The severe lattice distortion induced by the atomic size mismatch raises their potential energy, resulting in lower activation energy during catalytic processes [4]. Rationally, the catalytic activity of HEA-NPs/C was investigated for selective hydrogenation of phenol.

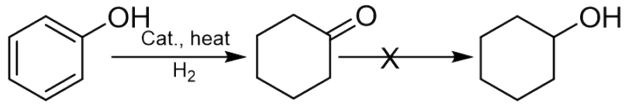

Scheme 2 Catalytic selective hydrogenation of phenol to cyclohexanone.

As seen in Table 1, HEA-NPs/C efficiently catalyzed phenol hydrogenation, yielding cyclohexanone as the predominant product. The phenol conversion was 88.7% within 1 h at 150 °C and 1 MPa H_2 pressure (Table 1, entry 1).

Table 1 Results of phenol hydrogenation by HEA-NPs/C under different conditions

Entry	Time (h)	H_2 pressure (MPa)	Conversion (%)	Selectivity C═O	Selectivity C—O
1	1	1.0	88.7	97.8	2.2
2	2.5	1.0	96.3	96.4	3.6
3	6	1.0	99.8	99.5	0.5
4	12	1.0	99.8	99.1	0.9
5	24	1.0	99.2	99.6	0.4
6	1	2.0	98.5	99.8	0.2

Reaction conditions: phenol (1.3 mmol), AuPdPtRhRu (10wt.% in HEA-NPs/C, 2.8 mol% relative to phenol; average molecular mass ≈ 140.5 g/mol), temperature = 150 °C, C═O denotes cyclohexanone and C—O denotes cyclohexanol.

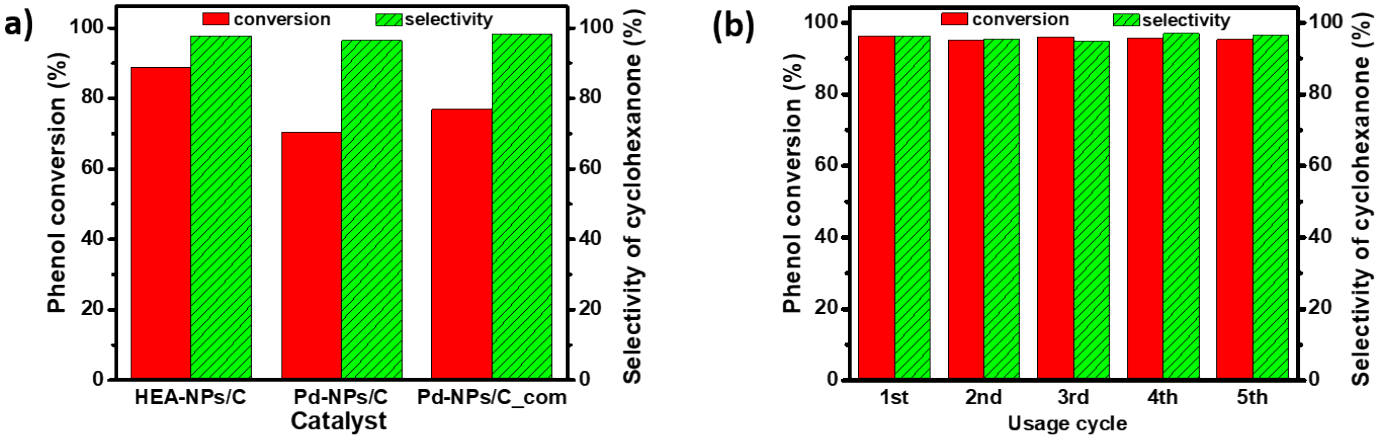

Figure 4 (a) Selective hydrogenation of phenol over different catalysts (1.3 mmol phenol, 2.8 mol% active metal (s) relative to phenol, 150 °C, 1 MPa H_2, 1 h). (b) reusability performance of HEA-NPs/C catalyst in phenol hydrogenation (1.3 mmol phenol, 2.8 mol% active metals relative to phenol, 150 °C, 2 MPa H_2, 1 h)

Upon increasing the reaction time to 2.5 h, the phenol conversion reached 96.3% with a cyclohexanone selectivity of 96.4%. Beyond 2.5 h reaction time, a close to 100% phenol conversion and cyclohexanone selectivity were achieved. Meanwhile, as the pressure was increased to 2.0 MPa, the conversion exceeded 98% within 1 h, with selectivity for cyclohexanone as high as 99.8% (Table 1, entry 6).

The relatively high selectivity of HEA-NPs/C is possibly due to the favorable desorption of cyclohexanone on the catalyst surface, inhibiting its further hydrogenation to cyclohexanol [56, 57]. Similar selectivity trend towards cyclohexanone production has also been demonstrated in other liquid-phase phenol hydrogenation catalyzed by Pd-based materials [58]. Under similar conditions, the catalytic performance of other multicomponent alloys investigated in the hydrogenation process decreased in the following order (Figure S9): quinary (AuPdPtRhRu) > quaternary (AuPdPtRh) > ternary (AuPdPt) > binary (AuPd). The configurational entropy of the multicomponent alloys increases with the addition of different elements; alloys in higher configurational entropy state demonstrate a higher synergistic effect, hence, superior catalytic performance.

Notably, a commercial Pd-NPs/C (Pd-NP/C_com) showed inferior catalytic performance relative to HEA-NPs/C but similar to as-synthesized Pd-NPs/C under similar reaction conditions. In Fig. 4(a), HEA-NPs/C displayed a phenol conversion of 88.7% at 150 °C with 1 MPa H_2 pressure within 1 h, which is higher than commercial Pd-NP/C_com (76.9%)

and as-synthesized Pd-NPs/C catalysts (70.5%) under the same reaction conditions. Meanwhile, the cyclohexanone selectivity over all three catalysts was virtually the same. Although Pd-based catalysts are predominantly used in selective hydrogenation of phenol, it is important to note that Pt [59-61], Rh [38, 62-64], and even Ru [65, 66] -based catalysts have all been investigated with satisfactory results (Table S2). Nevertheless, our HEA-NPs/C performed better than several noble metallic catalysts so far reported at relatively milder conditions [67-69]. For example, while Ru/γ-Al_2O_3 exhibited an 88% phenol conversion and 83% cyclohexanone selectivity at 160 °C, 2 h reaction time and 5 MPa H_2 pressure (Table S2, entry 1), our HEA-NPs/C catalyst showed a much higher phenol of 98.5 % and cyclohexanone selectivity of 99.8% at milder conditions (150 °C, 1 h reaction time and 2 MPa H_2 pressure). Similarly, HEA-NPs/C showed superior cyclohexanone selectivity of 99.8% compared to Rh/SiO_2 with 82.6% cyclohexanone selectivity (Table S2, entry 27). While there are a few single component noble metal catalysts that are more active and/or selective in reaction conditions that are milder than reported in the present work, it is important to note, however, that these single noble metal catalysts are often used in conjunction with Lewis acids as dual catalysts to activate the benzene ring and suppress further hydrogenation of cyclohexanone to cyclohexanol [40]. The superior catalytic performance of HEA-NPs/C is ascribed to the strong synergistic effect resulting from the combination of catalytically active metals. The numerous possible arrangements of different atoms on the catalyst surface may have provided different adsorption modes for phenol and its intermediate, hence the superior catalytic performance.

The recyclability of HEA-NPs/C was investigated through repeated hydrogenation experiments following a facile solvent wash process with acetone. As seen in Fig. 4(b), HEA-NPs/C demonstrated excellent stability, yielding phenol conversion and selectivity for cyclohexanone greater than 95% under the test conditions across all five usage cycles.

4 Conclusions

Summarily, we demonstrate a facile synthetic method to fabricate HEA-NP catalysts on a carbon support. Our methodology is based on the transient localized hotspot induced by the physical phenomenon of acoustic cavitation (formation, growth, and implosive collapse of microscopic bubbles in a liquid) observed in ultrasound irradiation of liquids. Owing to the reducing ability of alcohols, AILs were utilized as environmentally friendly reducing agent-cum-solvent in our strategy, co-reducing the precursor ions under high-intensity ultrasound irradiation in ambient conditions. The as-obtained NPs showed superior performance for selective hydrogenation of phenol compared to the monometallic counterparts due to the strong synergistic effects. Such a technologically feasible and facile synthetic method provides an improved methodology for the sustainable synthesis of multicomponent alloys for catalysis and other applications.

Acknowledgments

This work was supported by the Division of Chemical Sciences, Geosciences, and Biosciences, Office of Basic Energy Sciences, US Department of Energy. We also thank the Science Alliance for the Graduate Advancement, Training, and Education (GATE) scholarship award. We are truly grateful to Avery Blockmon for his contributions.

Electronic Supplementary Material: Supplementary material (ILs synthetic procedures, NMR spectra, EDS spectra, HAADF-STEM images, HR-STEM images, EDS elemental maps, phenol hydrogenation Table) is available in the online version of this article at http://dx.doi.org/10.1007/s12274-***-****-* (automatically inserted by the publisher)

References

[1] Fu, Z.; Jiang, L.; Wardini, J. L.; MacDonald, B. E.; Wen, H.; Xiong, W.; Zhang, D.; Zhou, Y.; Rupert, T. J.; Chen, W. et al. A high-entropy alloy with hierarchical nanoprecipitates and ultrahigh strength. *Sci. Adv.* **2018,** *4*, eaat8712.

[2] Yao, Y.; Liu, Z.; Xie, P.; Huang, Z.; Li, T.; Morris, D.; Finfrock, Z.; Zhou, J.; Jiao, M.; Gao, J. et al. Computationally aided, entropy-driven synthesis of highly efficient and durable multi-elemental alloy catalysts. *Sci. Adv.* **2020,** *6*, eaaz0510.

[3] Löffler, T.; Savan, A.; Garzón-Manjón, A.; Meischein, M.; Scheu, C.; Ludwig, A.; Schuhmann, W. Toward a paradigm shift in electrocatalysis using complex solid solution nanoparticles. *ACS Energy Lett.* **2019,** *4*, 1206-1214.

[4] Xin, Y.; Li, S.; Qian, Y.; Zhu, W.; Yuan, H.; Jiang, P.; Guo, R.; Wang, L. High-entropy alloys as a platform for catalysis: Progress, challenges, and opportunities. *ACS Catal.* **2020,** *10*, 11280-11306.

[5] Chen, H.; Jie, K.; Jafta, C. J.; Yang, Z.; Yao, S.; Liu, M.; Zhang, Z.; Liu, J.; Chi, M.; Fu, J. et al. An ultrastable heterostructured oxide catalyst based on high-entropy materials: A new strategy toward catalyst stabilization via synergistic interfacial interaction. *Appl. Catal., B* **2020,** *276*, 119155.

[6] Xu, H.; Zhang, Z.; Liu, J.; Do-Thanh, C.-L.; Chen, H.; Xu, S.; Lin, Q.; Jiao, Y.; Wang, J.; Wang, Y. et al. Entropy-stabilized single-atom pd catalysts via high-entropy fluorite oxide supports. *Nat. Commun.* **2020,** *11*.

[7] Shu, Y.; Bao, J.; Yang, S.; Duan, X.; Zhang, P. Entropy - stabilized metal - ceo x solid solutions for catalytic combustion of volatile organic compounds. *AlChE J.* **2021,** *67*.

[8] Feng, D.; Dong, Y.; Zhang, L.; Ge, X.; Zhang, W.; Dai, S.; Qiao, Z. A. Holey lamellar high - entropy oxide as an ultra - high - activity heterogeneous catalyst for solvent - free aerobic oxidation of benzyl alcohol. *Angew. Chem.* **2020,** *132*, 19671-19677.

[9] Yao, Y.; Huang, Z.; Xie, P.; Lacey, S. D.; Jacob, R. J.; Xie, H.; Chen, F.; Nie, A.; Pu, T.; Rehwoldt, M. et al. Carbothermal shock synthesis of high-entropy-alloy nanoparticles. *Science* **2018,** *359*, 1489.

[10] Chen, Y.; Zhan, X.; Bueno, S. L. A.; Shafei, I. H.; Ashberry, H. M.; Chatterjee, K.; Xu, L.; Tang, Y.; Skrabalak, S. E. Synthesis of monodisperse high entropy alloy nanocatalysts from core@shell nanoparticles. *Nanoscale Horiz.* **2021,** *6*, 231-237.

[11] Xie, P.; Yao, Y.; Huang, Z.; Liu, Z.; Zhang, J.; Li, T.; Wang, G.; Shahbazian-Yassar, R.; Hu, L.; Wang, C. Highly efficient decomposition of ammonia using high-entropy alloy catalysts. *Nat. Commun.* **2019,** *10*.

[12] Lv, Z. Y.; Liu, X. J.; Jia, B.; Wang, H.; Wu, Y.; Lu, Z. P. Development of a novel high-entropy alloy with eminent efficiency of degrading azo dye solutions. *Sci. Rep.* **2016,** *6*, 34213.

[13] Wu, S.-k.; Pan, Y.; Wang, N.; Lu, T.; Dai, W.-j. Azo dye degradation behavior of alfemntim (m = cr, co, ni) high-entropy alloys. *Int. J. Min. Met. Mater.* **2019,** *26*, 124-132.

[14] Qiu, H.-J.; Fang, G.; Wen, Y.; Liu, P.; Xie, G.; Liu, X.; Sun, S. Nanoporous high-entropy alloys for highly stable and efficient catalysts. *J. Mater. Chem. A* **2019,** *7*, 6499-6506.

[15] Zhang, G.; Ming, K.; Kang, J.; Huang, Q.; Zhang, Z.; Zheng, X.; Bi, X. High entropy alloy as a highly active and stable electrocatalyst for hydrogen evolution reaction. *Electrochim. Acta* **2018,** *279*, 19-23.

[16] Waag, F.; Li, Y.; Ziefuß, A. R.; Bertin, E.; Kamp, M.; Duppel, V.; Marzun, G.; Kienle, L.; Barcikowski, S.; Gökce, B. Kinetically-controlled laser-synthesis of colloidal high-entropy alloy nanoparticles. *RSC Adv.* **2019,** *9*, 18547-18558.

[17] Pedersen, J. K.; Batchelor, T. A. A.; Bagger, A.; Rossmeisl, J. High-entropy alloys as catalysts for the co2 and co reduction reactions. *ACS Catal.* **2020,** *10*, 2169-2176.

[18] Sun, Y.; Dai, S. High-entropy materials for catalysis: A new frontier. *Sci. Adv.* **2021,** *7*, eabg1600.

[19] Dai, S. Across the board: Sheng dai on catalyst design by entropic factors. *ChemSusChem* **2020,** *13*, 1915-1917.

[20] Wang, T.; Chen, H.; Yang, Z.; Liang, J.; Dai, S. High-entropy perovskite fluorides: A new platform for oxygen evolution catalysis. *J. Am. Chem. Soc.* **2020,** *142*, 4550-4554.

[21] Yang, Y.; Song, B.; Ke, X.; Xu, F.; Bozhilov, K. N.; Hu, L.; Shahbazian-Yassar, R.; Zachariah, M. R. Aerosol synthesis of high entropy alloy nanoparticles. *Langmuir* **2020,** *36*, 1985-1992.

[22] Gao, S.; Hao, S.; Huang, Z.; Yuan, Y.; Han, S.; Lei, L.; Zhang, X.; Shahbazian-Yassar, R.; Lu, J. Synthesis of high-entropy alloy nanoparticles on supports by the fast moving bed pyrolysis. *Nat. Commun.* **2020,** *11*, 2016.

[23] Joo, S. H.; Bae, J. W.; Park, W. Y.; Shimada, Y.; Wada, T.; Kim, H. S.; Takeuchi, A.; Konno, T. J.; Kato, H.; Okulov, I. V. Beating thermal coarsening in nanoporous materials via high - entropy design. *Adv. Mater.* **2020,** *32*, 1906160.

[24] Okulov, A. V.; Joo, S.-H.; Kim, H. S.; Kato, H.; Okulov, I. V. Nanoporous high-entropy alloy by liquid metal dealloying. *Metals* **2020,** *10*, 1396.

[25] Rekha, M. Y.; Mallik, N.; Srivastava, C. First report on high entropy alloy nanoparticle decorated graphene. *Sci. Rep.* **2018,** *8*.

[26] Löffler, T.; Meyer, H.; Savan, A.; Wilde, P.; Garzón Manjón, A.; Chen, Y.-T.; Ventosa, E.; Scheu, C.; Ludwig, A.; Schuhmann, W. Discovery of a multinary noble metal–free oxygen reduction catalyst. *Adv. Energy Mater.* **2018,** *8*, 1802269.

[27] Bondesgaard, M.; Broge, N. L. N.; Mamakhel, A.; Bremholm, M.; Iversen, B. B. General solvothermal synthesis method for complete solubility range bimetallic and high - entropy alloy nanocatalysts. *Adv. Funct. Mater.* **2019,** *29*, 1905933.

[28] Bang, J. H.; Suslick, K. S. Applications of ultrasound to the synthesis of nanostructured materials. *Adv. Mater.* **2010,** *22*, 1039-1059.

[29] Xu, H.; Zeiger, B. W.; Suslick, K. S. Sonochemical synthesis of nanomaterials. *Chem. Soc. Rev.* **2013,** *42*, 2555-2567.

[30] Okejiri, F.; Zhang, Z.; Liu, J.; Liu, M.; Yang, S.; Dai, S. Room-temperature synthesis of high-entropy perovskite oxide nanoparticle catalysts through ultrasonication-based method. *ChemSusChem* **2020,** *13*, 111-115.

[31] Liu, M.; Zhang, Z.; Okejiri, F.; Yang, S.; Zhou, S.; Dai, S. Entropy-maximized synthesis of multimetallic nanoparticle catalysts via a ultrasonication-assisted wet chemistry method under ambient conditions. *Adv. Mater. Interfaces* **2019,** *6*, 1900015.

[32] Kim, K.-S.; Choi, S.; Cha, J.-H.; Yeon, S.-H.; Lee, H. Facile one-pot synthesis of gold nanoparticles using alcohol ionic liquids. *J. Mater. Chem.* **2006,** *16*, 1315-1317.

[33] Yeon, S.-H.; Kim, K.-S.; Choi, S.; Lee, H.; Kim, H. S.; Kim, H. Physical and electrochemical properties of 1-(2-hydroxyethyl)-3-methyl imidazolium and n-(2-hydroxyethyl)-n-methyl morpholinium ionic liquids. *Electrochim. Acta* **2005,** *50*, 5399-5407.

[34] Anderson, J. L.; Clark, K. D. Ionic liquids as tunable materials in (bio)analytical chemistry. *Anal. Bioanal. Chem.* **2018,** *410*, 4565-4566.

[35] Wu, Q.; Hong, X.; Zhu, L.; Meng, X.; Han, S.; Zhang, J.; Liu, X.; Jin, C.; Xiao, F.-S. Generalized ionothermal synthesis of silica-based zeolites. *Microporous Mesoporous Mater.* **2019,** *286*, 163-168.

[36] Zhang, P.; Gong, Y.; Lv, Y.; Guo, Y.; Wang, Y.; Wang, C.; Li, H. Ionic liquids with metal chelate anions. *Chem. Commun.* **2012,** *48*, 2334.

[37] Lu, H.; Zhang, P.; Qiao, Z.-A.; Zhang, J.; Zhu, H.; Chen, J.; Chen, Y.; Dai, S. Ionic liquid-mediated synthesis of meso-scale porous lanthanum-transition-metal perovskites with high co oxidation performance. *Chem. Commun.* **2015,** *51*, 5910-5913.

[38] Fujita, S.-i.; Yamada, T.; Akiyama, Y.; Cheng, H.; Zhao, F.; Arai, M. Hydrogenation of phenol with supported rh catalysts in the presence of compressed co2: Its effects on reaction rate, product selectivity and catalyst life. *J. Supercrit. Fluids* **2010,** *54*, 190-201.

[39] Xiang, Y.; Ma, L.; Lu, C.; Zhang, Q.; Li, X. Aqueous system for the improved hydrogenation of phenol and its derivatives. *Green Chem.* **2008,** *10*, 939-943.

[40] Liu, H.; Jiang, T.; Han, B.; Liang, S.; Zhou, Y. Selective phenol hydrogenation to cyclohexanone over a dual supported pd–lewis acid catalyst. *Science* **2009,** *326*, 1250.

[41] Mahata, N.; Raghavan, K. V.; Vishwanathan, V.; Park, C.; Keane, M. A. Phenol hydrogenation over palladium supported on magnesia: Relationship between catalyst structure and performance. *Phys. Chem. Chem. Phys.* **2001,** *3*, 2712-2719.

[42] Chatterjee, M.; Kawanami, H.; Sato, M.; Chatterjee, A.; Yokoyama, T.; Suzuki, T. Hydrogenation of phenol in supercritical carbon dioxide catalyzed by palladium supported on al-mcm-41: A facile route for one-pot cyclohexanone formation. *Adv. Synth. Catal.* **2009,** *351*, 1912-1924.

[43] Nelson, N. C.; Manzano, J. S.; Sadow, A. D.; Overbury, S. H.; Slowing, I. I. Selective hydrogenation of phenol catalyzed by palladium on high-surface-area ceria at room temperature and ambient pressure. *ACS Catal.* **2015,** *5*, 2051-2061.

[44] Mahata, N.; Vishwanathan, V. Influence of palladium precursors on structural properties and phenol hydrogenation characteristics of supported palladium catalysts. *J. Catal.* **2000,** *196*, 262-270.

[45] Xu, G.; Guo, J.; Zhang, Y.; Fu, Y.; Chen, J.; Ma, L.; Guo, Q. Selective hydrogenation of phenol to cyclohexanone over pd-hap catalyst in aqueous media. *ChemCatChem* **2015,** *7*, 2485-2492.

[46] Zhu, J.-F.; Tao, G.-H.; Liu, H.-Y.; He, L.; Sun, Q.-H.; Liu, H.-C. Aqueous-phase selective hydrogenation of phenol to cyclohexanone over soluble pd nanoparticles. *Green Chem.* **2014,** *16*, 2664-2669.

[47] Liu, S.; Han, J.; Wu, Q.; Bian, B.; Li, L.; Yu, S.; Song, J.; Zhang, C.; Ragauskas, A. J. Hydrogenation of phenol to cyclohexanone over bifunctional pd/c-heteropoly acid catalyst in the liquid phase. *Catal. Lett.* **2019,** *149*, 2383-2389.

[48] Makowski, P.; Demir Cakan, R.; Antonietti, M.; Goettmann, F.; Titirici, M.-M. Selective partial hydrogenation of hydroxy aromatic derivatives with palladium nanoparticles supported on hydrophilic carbon. *Chem. Commun.* **2008**, 999.

[49] Chen, H.; Sun, J. Selective hydrogenation of phenol for cyclohexanone: A review. *J. Ind. Eng. Chem.* **2021,** *94*, 78-91.

[50] Srinivas, S. T.; Rao, P. K. Highly selective pt–cr/c alloy catalysts for single-step vapour phase hydrogenation of phenol to give cyclohexanone. *J. Chem. Soc., Chem. Commun.* **1993,** *0*, 33-34.

[51] Shore, S. G.; Ding, E.; Park, C.; Keane, M. A. Vapor phase hydrogenation of phenol over silica supported pd and pd□yb catalysts. *Catal. Commun.* **2002,** *3*, 77-84.

[52] Yang, X.; Du, L.; Liao, S.; Li, Y.; Song, H. High-performance gold-promoted palladium catalyst towards the hydrogenation of phenol with mesoporous hollow spheres as support. *Catal. Commun.* **2012,** *17*, 29-33.

[53] Lin, H.; Muzzio, M.; Wei, K.; Zhang, P.; Li, J.; Li, N.; Yin, Z.; Su, D.; Sun, S. Pdau alloy nanoparticles for ethanol oxidation in alkaline conditions: Enhanced activity and c1 pathway selectivity. *ACS Appl. Energy Mater.* **2019,** *2*, 8701-8706.

[54] Muzzio, M.; Yu, C.; Lin, H.; Yom, T.; Boga, D. A.; Xi, Z.; Li, N.; Yin, Z.; Li, J.; Dunn, J. A. et al. Reductive amination of ethyl levulinate to pyrrolidones over aupd nanoparticles at ambient hydrogen pressure. *Green Chem.* **2019,** *21*, 1895-1899.

[55] Wang, L.; He, S.; Wang, L.; Lei, Y.; Meng, X.; Xiao, F.-S. Cobalt–nickel catalysts for selective hydrogenation of carbon dioxide into ethanol. *ACS Catal.* **2019,** *9*, 11335-11340.

[56] Zhong, J.; Chen, J.; Chen, L. Selective hydrogenation of phenol and related derivatives. *Catal. Sci. Technol.* **2014,** *4*, 3555-3569.

[57] Scirè, S.; Minicò, S.; Crisafulli, C. Selective hydrogenation of phenol to cyclohexanone over supported pd and pd-ca catalysts: An investigation on the influence of different supports and pd precursors. *Appl. Catal., A* **2002,** *235*, 21-31.

[58] Kong, X.; Gong, Y.; Mao, S.; Wang, Y. Selective hydrogenation of phenol. *ChemNanoMat* **2018,** *4*, 432-450.

[59] Talukdar, A. K.; Bhattacharyya, K. G.; Sivasanker, S. Hydrogenation of phenol over supported platinum and palladium catalysts. *Appl. Catal., A* **1993,** *96*, 229-239.

[60] Yang, X.; Yu, X.; Long, L.; Wang, T.; Ma, L.; Wu, L.; Bai, Y.; Li, X.; Liao, S. Pt nanoparticles entrapped in titanate nanotubes (tnt) for phenol hydrogenation: The confinement effect of tnt. *Chem. Commun.* **2014,** *50*, 2794.

[61] Srinivas, S. T.; Kanta Rao, P. Synthesis, characterization and activity studies of carbon supported platinum alloy catalysts. *J. Catal.* **1998,** *179*, 1-17.

[62] Giraldo, L.; Bastidas-Barranco, M.; Moreno-Piraján, J. Vapour phase hydrogenation of phenol over rhodium on sba-15 and sba-16. *Molecules* **2014,** *19*, 20594-20612.

[63] Martinez-Espinar, F.; Blondeau, P.; Nolis, P.; Chaudret, B.; Claver, C.; Castillón, S.; Godard, C. Nhc-stabilised rh nanoparticles: Surface study and application in the catalytic hydrogenation of aromatic substrates. *J. Catal.* **2017,** *354*, 113-127.

[64] Rode, C. V.; Joshi, U. D.; Sato, O.; Shirai, M. Catalytic ring hydrogenation of phenol under supercritical carbon dioxide. *Chem. Commun.* **2003**, 1960.

[65] Raut, A. N.; Nandanwar, S. U.; Suryawanshi, Y. R.; Chakraborty, M.; Jauhari, S.; Mukhopadhyay, S.; Shenoy, K. T.; Bajaj, H. C. Liquid phase selective hydrogenation of phenol to cyclohexanone over ru/al2o3 nanocatalyst under mild conditions. *Kinet. Catal.* **2016,** *57*, 39-46.

[66] Vinokurov, V.; Glotov, A.; Chudakov, Y.; Stavitskaya, A.; Ivanov, E.; Gushchin, P.; Zolotukhina, A.; Maximov, A.; Karakhanov, E.; Lvov, Y. Core/shell ruthenium–halloysite nanocatalysts for hydrogenation of phenol. *Ind. Eng. Chem. Res.* **2017,** *56*, 14043-14052.

[67] Raspolli Galletti, A. M.; Antonetti, C.; Giaiacopi, S.; Piccolo, O.; Venezia, A. M. Innovative process for the synthesis of nanostructured ruthenium catalysts and their catalytic performance. *Top. Catal.* **2009,** *52*, 1065-1069.

[68] Raspolli Galletti, A. M.; Antonetti, C.; Longo, I.; Capannelli, G.; Venezia, A. M. A novel microwave assisted process for the synthesis of nanostructured ruthenium catalysts active in the hydrogenation of phenol to cyclohexanone☆. *Appl. Catal., A* **2008,** *350*, 46-52.

[69] Zhang, H.; Han, A.; Okumura, K.; Zhong, L.; Li, S.; Jaenicke, S.; Chuah, G.-K. Selective hydrogenation of phenol to cyclohexanone by sio2-supported rhodium nanoparticles under mild conditions. *J. Catal.* **2018,** *364*, 354-365.

Electronic Supplementary Material

Ultrasound-driven fabrication of high-entropy alloy nanocatalysts promoted by alcoholic ionic liquids

Francis Okejiri[1,2], Zhenzhen Yang[2] (✉), Hao Chen[1], Chi-Linh Do-Thanh[1], Tao Wang[2], Shize Yang[3,†] (✉), Sheng Dai[1,2] (✉)

[1] *Department of Chemistry, The University of Tennessee, Knoxville, TN 37996, USA*
[2] *Chemical Sciences Division, Oak Ridge National Laboratory, Oak Ridge, TN 37831, USA*
[3] *Center for Functional Nanomaterials, Brookhaven National Laboratory, Upton, New York 11973, USA*
[†] *Eyring Materials Center, Arizona State University, Tempe, AZ 85287, USA*

Supporting information to DOI 10.1007/s12274-****-****-* (automatically inserted by the publisher)

Table of Contents

Address correspondence to Sheng Dai, dais@ornl.gov; Zhenzhen Yang, yangz3@ornl.gov; Shize Yang, syang212@asu.edu

Materials:

All the chemical reagents used in this work were of analytical grade. Potassium tetrachloropalladate (II) (K_2PdCl_4), potassium tetrachloroplatinate (II) (K_2PtCl_4), ruthenium chloride ($RuCl_3$), gold chloride hydrate ($HAuCl_4 \cdot 3H_2O$), rhodium chloride ($RhCl_3$), ethylene glycol ($HO\text{-}CH_2CH_2\text{-}OH$), acetone ($CH_3\text{-}CO\text{-}CH_3$), cyclohexanone ($(CH_2)_2CO$), commercial Pd/carbon catalyst (Pd weight loading - 10 %), acetonitrile (CH_3CN) were purchased from Fisher Chemicals. N-methylmorpholine ($O(CH_2CH_2)_2NCH_3$), phenol (C_6H_5OH), cyclohexanol ($HOCH(CH_2)5$), 2-bromoethanol ($BrCH_2CH_2OH$), bromoethane ($BrCH_2CH_3$), acetonitrile (CH_3CN), ethyl ether ($(CH_3CH_2)_2O$), and ethyl acetate ($CH_3COOC_2H_5$), were acquired from ACROS ORGANICS. Lithium bis(trifluoromethane)sulfonimide ($LiNTf_2$), sodium tetrafluoroborate ($NaBF_4$), and activated charcoal were purchased from Sigma-Aldrich. Carbon (Vulcan XC-72R) was bought from the Fuel Cell Store. All the chemicals were used without further purification.

Synthesis of ethyl-N-methylmorpholinium bis(trifluoromethylsulfonyl)imide - [EMMor][NTf_2]:

N-methylmorpholine (0.55 mol) and excess bromoethane (0.60 mol) were mixed with 300 mL acetonitrile in a round-bottom flask and stirred at 90 °C for 12 h under an N_2 atmosphere. The solvent was removed under reduced pressure, and the residue was washed with ethyl ether to obtain ethyl-N-methylmorpholinium bromide ([EMMor][Br]) as a crystalline solid. The solid was redissolved in 300 mL deionized water (DI) and decolorized with activated charcoal by refluxing overnight. The aqueous layer was recovered by vacuum filtration and used for the anionic exchange with $LiNTf_2$ (0.55mol) at room temperature. The non-aqueous layer was extracted in ethyl acetate and dried under removed pressure to obtain [EMMor][NTf_2]. The reaction scheme is shown below. The structure was characterized by NMR spectroscopy, and the following peak positions were observed. ^{1}H NMR (400 MHz, DMSO-d_6, δ/ppm, relative to TMS): δ 1.22 - 1.28 (t, 3H), 3.05(s, 3H), 3.34 – 3.36 (t, 4H), 3.45 – 3.54 (q, 2H), 3.88 – 3.98 (s, 4H).

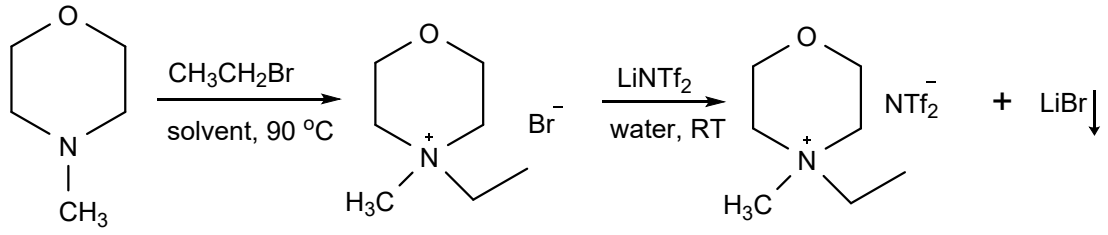

Scheme S1 Synthesis of [EMMor][NTf_2]

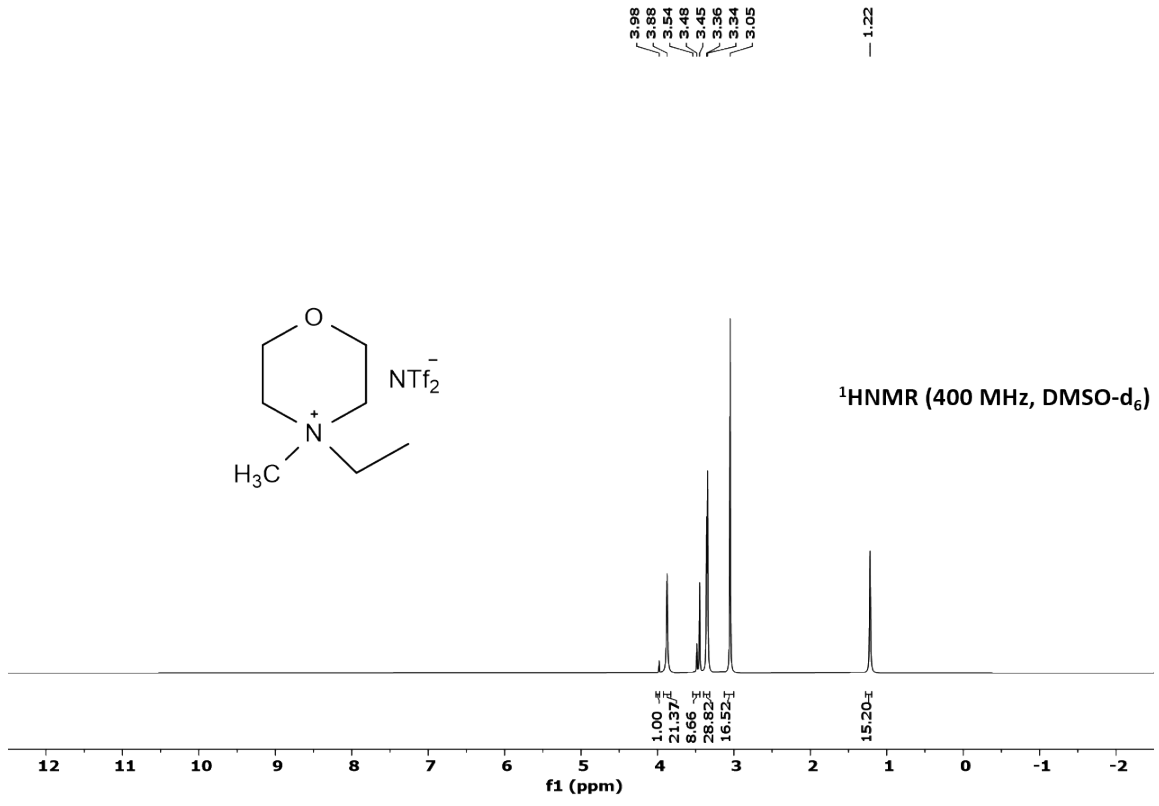

Figure S1 NMR spectrum of [EMMor][NTf_2]

Synthesis of N-(2-hydroxyethyl)-N-methylmorpholinium tetrafluoroborate – [HEMMor]BF_4]:
[HEMMor]BF_4] was synthesized according to previous reports with some modifications. N-methylmorpholine (0.55 mol) and excess 2-bromoethanol (0.60 mol) were mixed with 300 mL acetonitrile in a round-bottom flask and stirred at 90 °C for 12 h under an N_2 atmosphere. The solvent was removed under reduced pressure, and the residue was washed with ethyl ether to obtain ethyl-N-methylmorpholinium bromide ([HEMMor][Br]) as a crystalline solid. The solid was redissolved in 300 mL deionized water (DI) and decolorized with activated charcoal by refluxing overnight. The aqueous layer was recovered by vacuum filtration and used for the anionic exchange with $NaBF_4$ (0.55mol) at room temperature. The residual of NaBr was removed from the ionic liquid by low-temperature filtration.The reaction scheme is shown below. The structure was characterized by NMR spectroscopy, and the following peak positions were observed. ^{1}H NMR (400 MHz, DMSO-d_6, δ/ppm, relative to TMS): δ 3.18 (s, 3H), 3.43 (t, 2H), 3.55 (t, 2H), 3.61 (t, 2H), 3.81 (s, 2H), 3.87 (s, 4H), 5.29 (t, 1H).

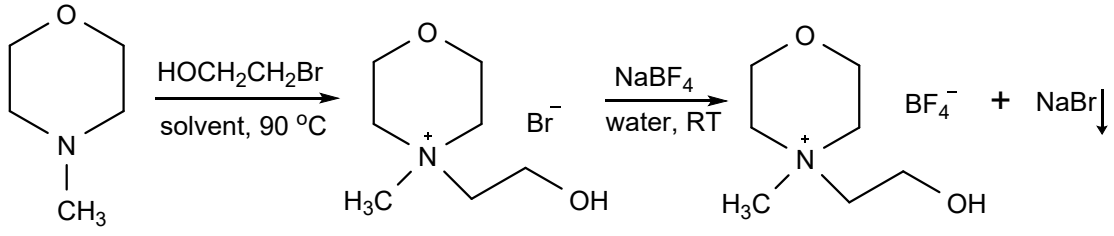

Scheme S2 Synthesis of [HEMMor][BF_4]

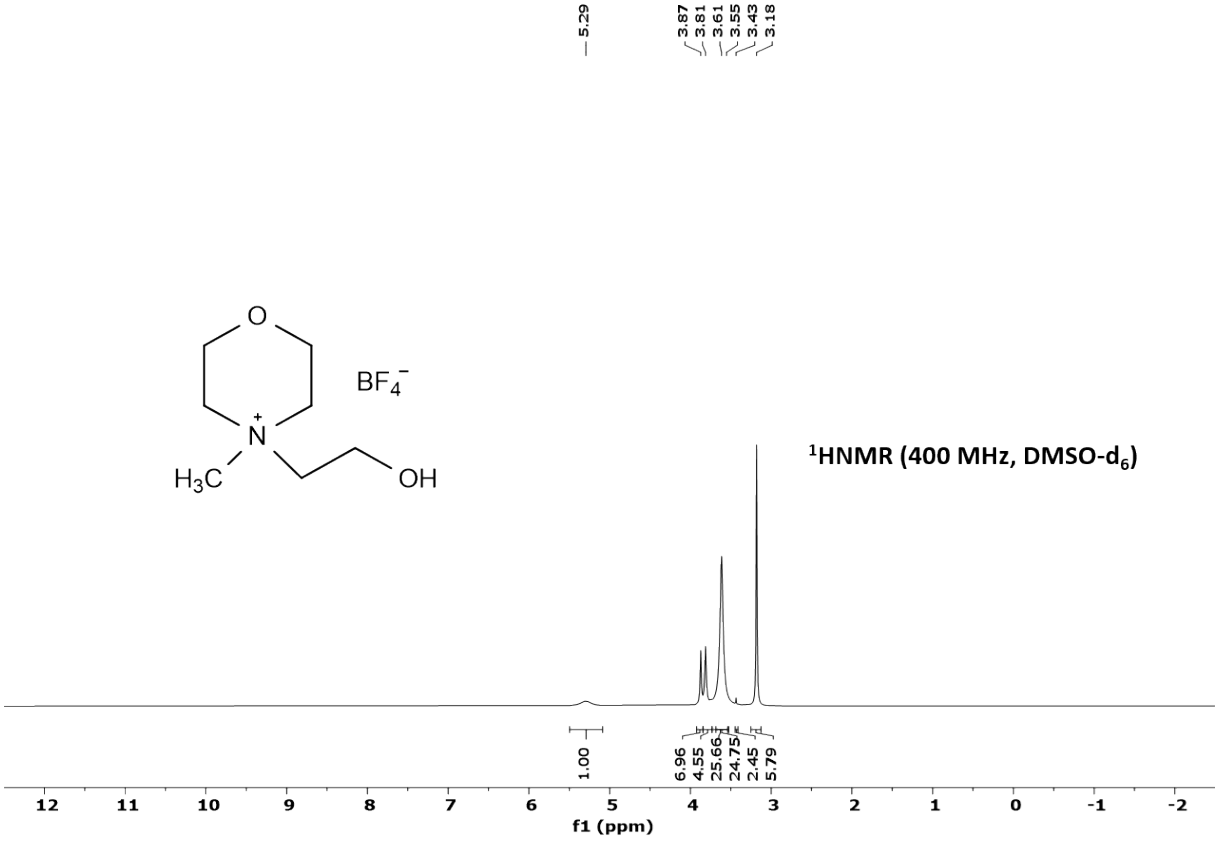

Figure S2 NMR spectrum of [HEMMor][BF_4]

Synthesis and characterization of N-(2-hydroxyethyl)-N-methylmorpholinium bis(trifluoromethylsulfonyl)imide) – [HEMMor][NTf_2]:

HEMMor][NTf_2] was synthesized according to the procedure described in the main text. The reaction scheme is shown belo. The structure was characterized by NMR spectroscopy and the following peak positions were observed. ^{1}H NMR (400 MHz, DMSO-d_6, δ/ppm, relative to TMS): δ 3.20 (s, 3H), 3.45 (t, 2H), 3.58 (t, 2H), 3.60 (t, 2H), 3.80 (s, 2H), 3.89 (s, 4H), 5.28 (t, 1H).

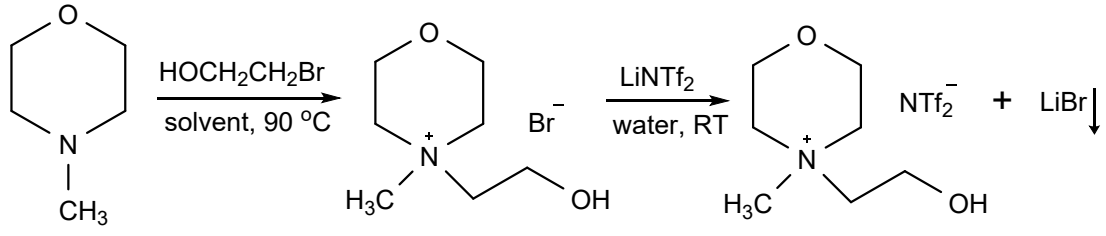

Scheme S3 Synthesis of [HEMMor][NTf_2]

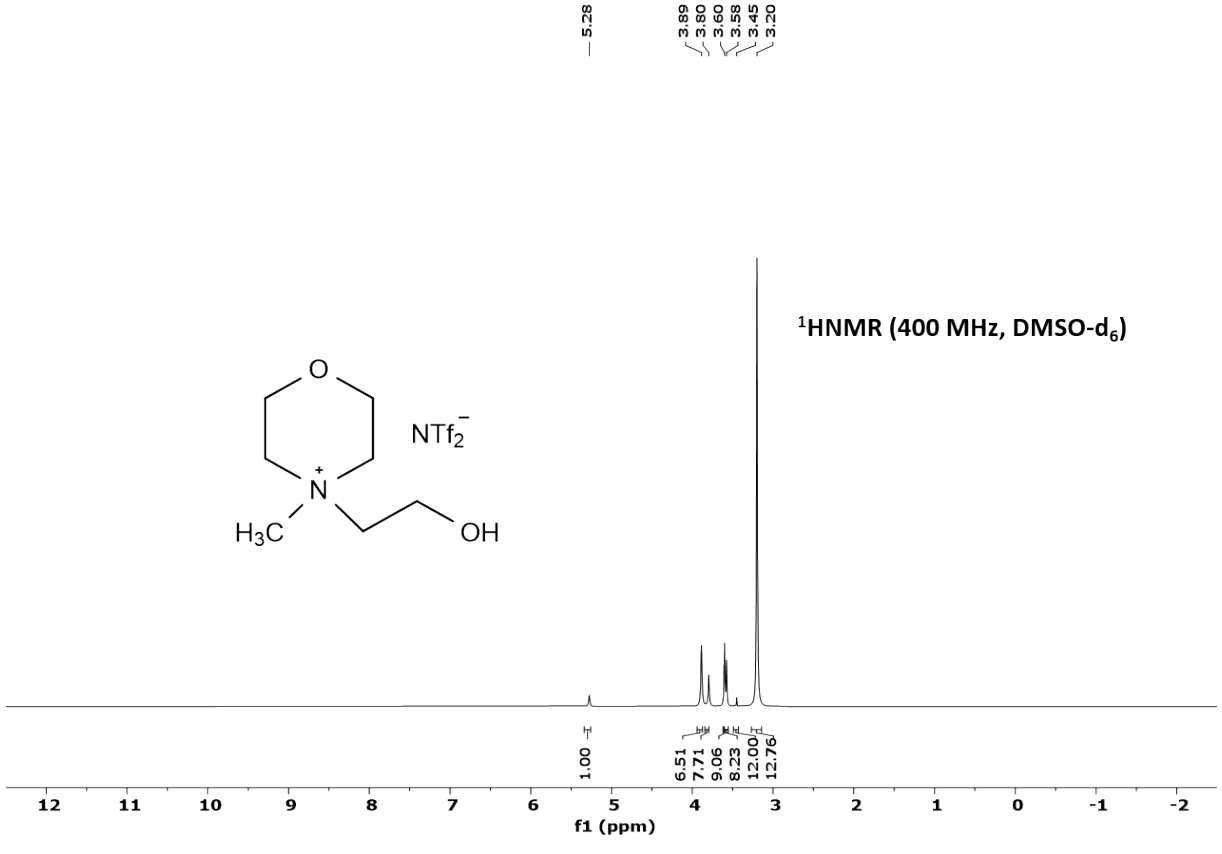

Figure S3 NMR spectrum of [HEMMor][NTf_2]

Synthesis of Pd-NPs/C:
K_2PdCl_4 (0.025 mmol) was dissolved in a minimum volume of DI water to form a salt solution. This solution was combined with a calculated mass of XC-72 carbon support pre-dispersed in 30mL IL for a total metal loading of 10wt.%. The mixture was exposed to sonication treatment for 10 min by direct immersion of ultrasonic titanic horn operating at 20 kHz at ambient conditions. When the sonication time was reached, the solid was recovered by centrifugation and washed thoroughly with DI before being dried in an oven at 100 °C overnight.

Synthesis of Au-NPs/C:
$HAuCl_4 \cdot 3H_2O$ (0.025 mmol) was dissolved in a minimum volume of DI water to form a salt solution. This solution was combined with a calculated mass of XC-72 carbon support pre-dispersed in 30mL IL for a total metal loading of 10wt.%. The mixture was exposed to sonication treatment for 10 min by direct immersion of ultrasonic titanic horn operating at 20 kHz at ambient conditions. When the sonication time was reached, the solid was recovered by centrifugation and washed thoroughly with DI before being dried in an oven at 100 °C overnight.

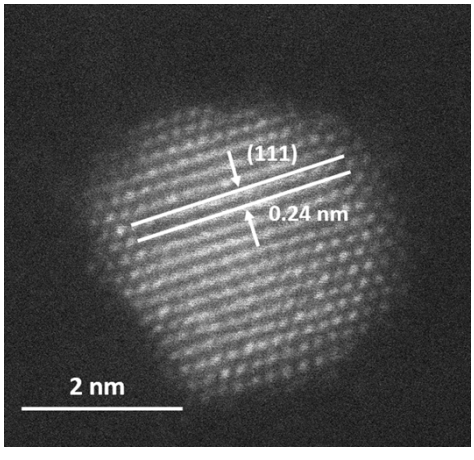

Figure S4 HR-STEM image of the supported high-entropy alloy nanoparticle catalyst (HEA-NP/C) showing a lattice fringe spacing of 0.24 nm consistent with the (111) plane of a face-centered cubic crystal structure.

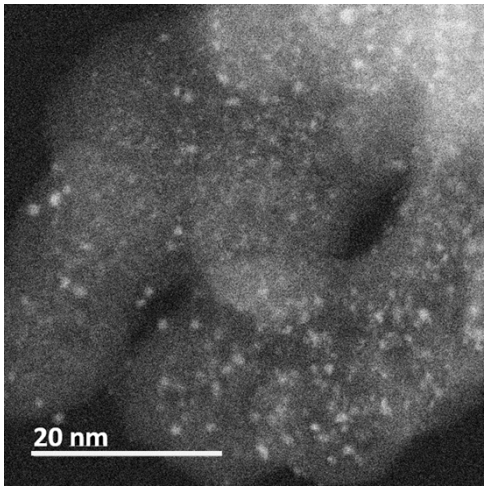

Figure S5 STEM image of the supported high-entropy alloy nanoparticle catalysts (HEA-NP/C) displaying ultra-small-sized particles of AuPdPdPtRhRh dispersed on the carbon support.

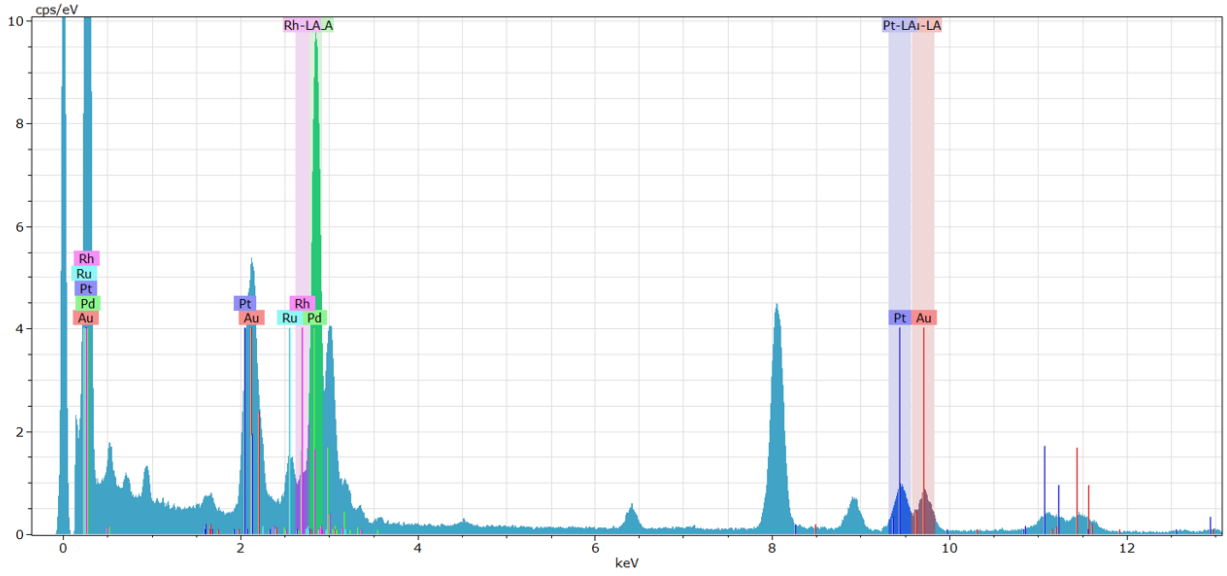

Figure S6 EDS spectrum of the supported high-entropy alloy nanoparticle catalysts (HEA-NP/C) showing the constituent elements.

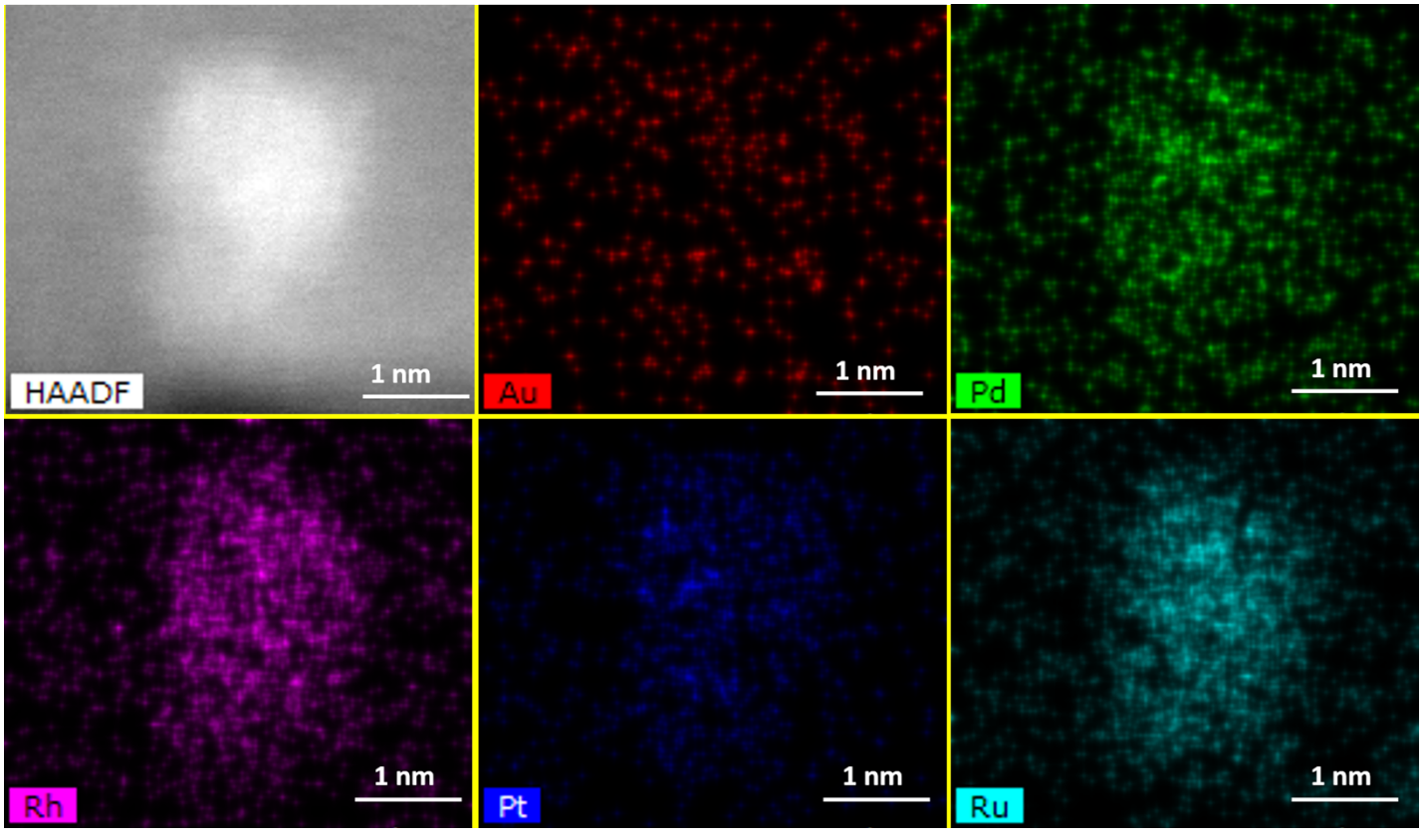

Figure S7 HAADF image and EDS elemental maps of the supported high-entropy alloy nanocatalyst (HEA-NPs/C) synthesized via the ultrasound-driven wet chemistry method promoted by alcoholic ionic liquid (AIL).

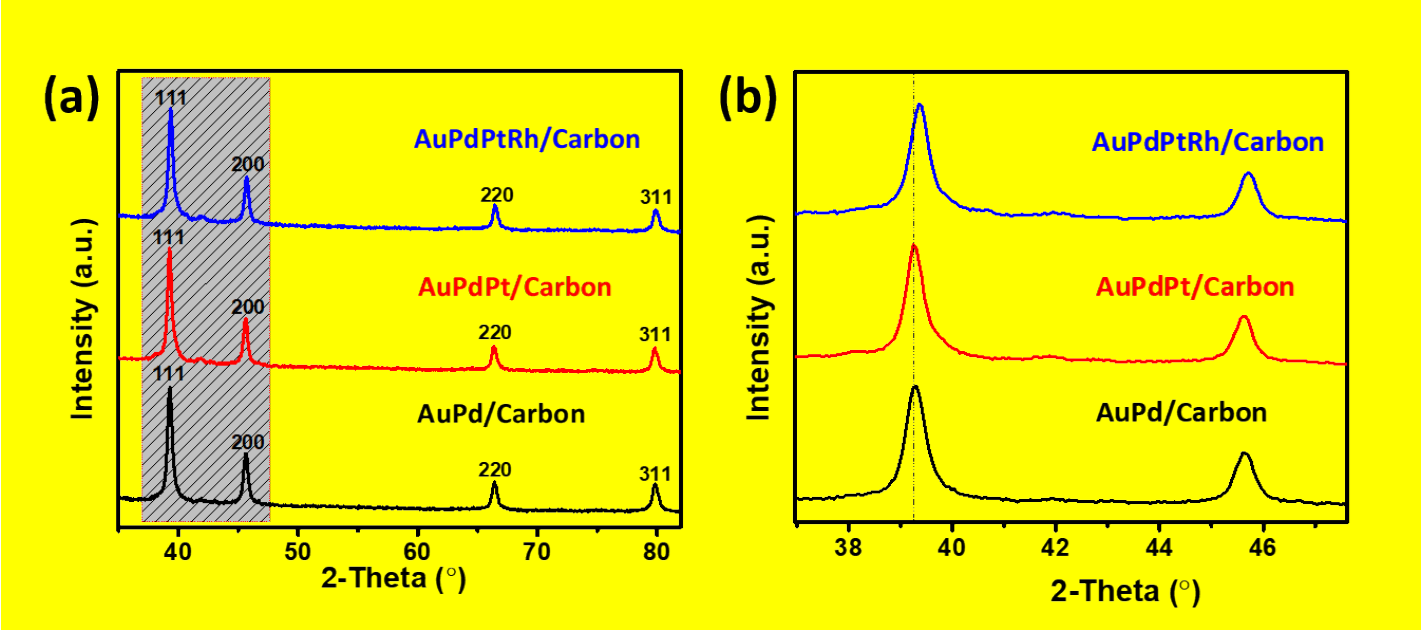

Figure S8 (a) XRD patterns of supported multicomponent alloy nanocatalysts synthesized via the ultrasound-driven wet chemistry method promoted by alcoholic ionic liquid (AIL). The shift in reflection positions with the addition of more element is denoted by the dotted lines in (b).

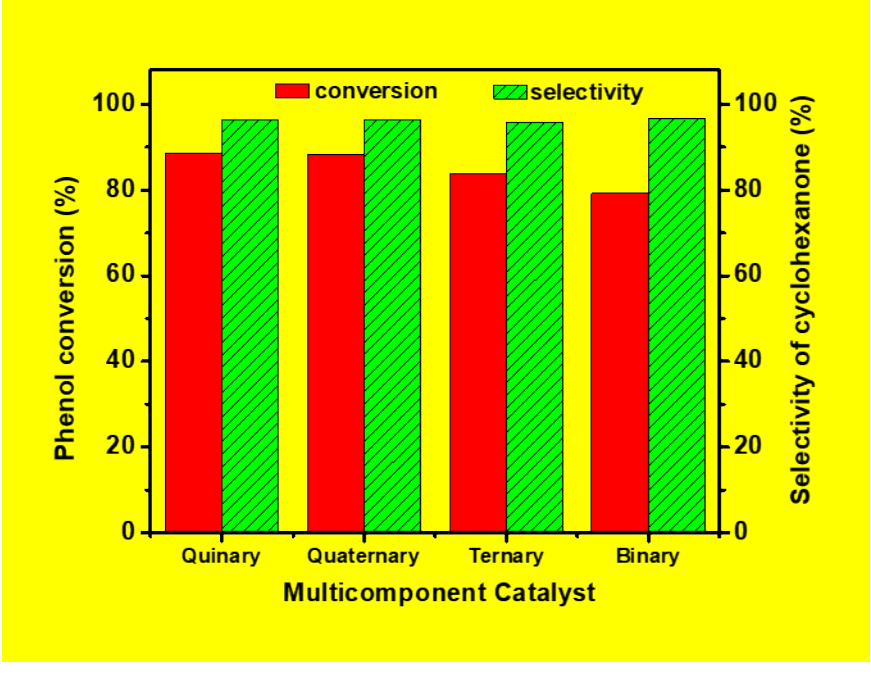

Figure S9 Selective hydrogenation of phenol over different multicomponent catalysts (quinary (AuPdPtRhRu), quaternary (AuPdPtRh), ternary (AuPdPt), binary (AuPd), 1.3 mmol phenol, 2.8 mol% active metals relative to phenol, 150 °C, 1 MPa H_2, 1 h).

Table S1 Summary of HEA catalysts for thermally-driven and electrocatalytic applications.

Catalyst	Synthetic method	Structure	Catalytic reaction	Ref.
AuPdPtRhRu	Ultrasonication	fcc	Phenol hydrogenation	This work
PtPdRhRuCe	Carbothermal shock	fcc	NH_3 oxidation	[1]
AgIrPdPtRu	Sputtering	fcc	ORR	[2]
PtNiFeCoCu	Colloidal Synthesis	fcc	HER and alcohol oxidation	[3]
AlNiCoIrMo	Dealloying	fcc	OER	[4]
MnFeCoNiCu	Solvothermal	fcc	OER	[5]
CoCrFeMnNi	Laser ablation	fcc	OER	[6]
FeCoPdIrPt	Fast-moving bed pyrolysis	fcc	HER	[7]
IrPdPtRhRu	Polyol method	fcc	HER	[8]
CoFeLaNiPt	Electrodeposition	Amorphous	OER and HER	[9]
AuAgPtPdCu	Melting-cryogrinding	fcc	CO_2 reduction	[10]
IrOsReRhRu	Thermal decomposition	hcp	Alcohol oxidation	[11]

Table S2 Summary of hydrogenation of phenol to cyclohexanone over noble metal-based catalysts

Catalyst	Solvent	Reactor	Temp. (°C)	Time (h)	H_2 pressure (MPa)	Conversion (%)	Selectivity (%)	Ref.
9.7 wt% AuPdPtRhRu/C	Hexane	Autoclave	150	2.5	1	96.3	96.4	This work
9.7 wt% AuPdPtRhRu/C	Hexane	Autoclave	150	1	2	98.5	99.8	This work
5.0 wt% Ru/γ-Al_2O_3	Cyclohexane	Autoclave	160	2	5	88	83	[12]
5.0 wt% Ru/MIL-101	CH_2Cl_2	Batch reactor	50	4	0.5	80	74	[13]
5.0 wt% Ru/MIL-101	H_2O	Batch reactor	50	4	0.5	90	90	[13]
Pd/mpg-C_3N_4	H_2O		45	12	0.1	99	98.5	[14]
Pd/mpg-C_3N_4	H_2O		100	1	0.1	99	99	[14
Pd–Ca/La_2O_3	C_2H_5OH	Tubular reactor	220		0.1	52	93	[15]
Pd–Ca/CeO_2	C_2H_5OH	Tubular reactor	220		0.1	55	92	[15]
Pd–Ca/Al_2O_3	C_2H_5OH	Tubular reactor	220		0.1	38	93	[15]
5 wt%Ru/γ-Al_2O_3	Cyclohexane	Autoclave	160	3	5	100	90	[16]
2.7 wt%Pd/A-45	H_2O	Reactor	100	3	1	100	89.9	[17]
2.2 wt%Rh@S-MIL-101	CH_2Cl_2	Batch reactor	50	2	0.5	91	85	[18]
5 wt%Pd/MIL-101	H_2O	Autoclave	25	11	0.1	99.9	99.9	[19]
2 mol%Pd/C	H_2O, HCOOK	Round bottom flask	90	6	Open atmosphere	99	99	[20]
Rh	Cyclodextrins		60	3	4	88	100	[21]
5 wt%Pd/Al_2O_3	CH_2Cl_2		30	12	1	15.5	89.5	[22]
5 wt%Pd/Al_2O_3, $AlCl_3$	CH_2Cl_2		30	8	1	99.9	99.9	[22]
2 mol%Pd/C	H_2O, HCOOK	Round bottom flask	90	6	Open atmosphere	99	99	[21]
8.1 wt% Rh@SiCN	GVL, H_2O	Steel autoclave	25	4	0.6	67	72	[23]
8.1 wt% Rh@SiCN	H_2O	Steel autoclave	25	2	0.6	54	67	[23]
8.1 wt% Rh@SiCN	CH_3COCH_3, H_2O	Steel autoclave	25	2	0.6	37	82	[23]
2.2 wt%Rh@S-MIL-101	H_2O	Batch reactor	50	2	0.5	95	92	[18]
0.6 wt%Ru@NaX	H_2O	Three-necked flask	80	10	0.1	90	99.9	[24]
1 wt%Pd–HAP	H_2O	Tube	75	3	0.1	100	100	[25]
1 wt%Pt@TNT	CH_2Cl_2	Autoclave	50		0.5	95	83	[26]
5 wt%Rh/SiO_2	Cyclohexane	Autoclave	30	9	0.1	100	82.6	[27]
Pd/CNTs	CH_3OH	Tubular reactor	220		3.5[a]	18	99	[28]
3 wt%Pt-out/CNTs	CH_2Cl_2	Autoclave	50	0.5	0.5	11.6	72.3	[29]

[a] Argon pressure.

References

[1] Yao, Y.; Huang, Z.; Xie, P.; Lacey, S. D.; Jacob, R. J.; Xie, H.; Chen, F.; Nie, A.; Pu, T.; Rehwoldt, M. et al. Carbothermal shock synthesis of high-entropy-alloy nanoparticles. *Science* **2018,** *359*, 1489.

[2] Batchelor, T. A. A.; Löffler, T.; Xiao, B.; Krysiak, O. A.; Strotkötter, V.; Pedersen, J. K.; Clausen, C. M.; Savan, A.; Li, Y.; Schuhmann, W. et al. Complex-solid-solution electrocatalyst discovery by computational prediction and high-throughput experimentation**. *Angew. Chem. Int. Ed.* **2021,** *60*, 6932-6937.

[3] Chen, Y.; Zhan, X.; Bueno, S. L. A.; Shafei, I. H.; Ashberry, H. M.; Chatterjee, K.; Xu, L.; Tang, Y.; Skrabalak, S. E. Synthesis of monodisperse high entropy alloy nanocatalysts from core@shell nanoparticles. *Nanoscale Horiz.* **2021,** *6*, 231-237.

[4] Jin, Z.; Lv, J.; Jia, H.; Liu, W.; Li, H.; Chen, Z.; Lin, X.; Xie, G.; Liu, X.; Sun, S. et al. Nanoporous al-ni-co-ir-mo high-entropy alloy for record-high water splitting activity in acidic environments. *Small* **2019,** *15*, 1904180.

[5] Huang, K.; Zhang, B.; Wu, J.; Zhang, T.; Peng, D.; Cao, X.; Zhang, Z.; Li, Z.; Huang, Y. Exploring the impact of atomic lattice deformation on oxygen evolution reactions based on a sub-5 nm pure face-centred cubic high-entropy alloy electrocatalyst. *J. Mater. Chem. A* **2020,** *8*, 11938-11947.

[6] Waag, F.; Li, Y.; Ziefuß, A. R.; Bertin, E.; Kamp, M.; Duppel, V.; Marzun, G.; Kienle, L.; Barcikowski, S.; Gökce, B. Kinetically-controlled laser-synthesis of colloidal high-entropy alloy nanoparticles. *RSC Adv.* **2019,** *9*, 18547-18558.

[7] Gao, S.; Hao, S.; Huang, Z.; Yuan, Y.; Han, S.; Lei, L.; Zhang, X.; Shahbazian-Yassar, R.; Lu, J. Synthesis of high-entropy alloy nanoparticles on supports by the fast moving bed pyrolysis. *Nat. Commun.* **2020,** *11*, 2016.

[8] Wu, D.; Kusada, K.; Yamamoto, T.; Toriyama, T.; Matsumura, S.; Gueye, I.; Seo, O.; Kim, J.; Hiroi, S.; Sakata, O. et al. On the electronic structure and hydrogen evolution reaction activity of platinum group metal-based high-entropy-alloy nanoparticles. *Chemical Science* **2020,** *11*, 12731-12736.

[9] Glasscott, M. W.; Pendergast, A. D.; Goines, S.; Bishop, A. R.; Hoang, A. T.; Renault, C.; Dick, J. E. Electrosynthesis of high-entropy metallic glass nanoparticles for designer, multi-functional electrocatalysis. *Nat. Commun.* **2019,** *10*.

[10] Nellaiappan, S.; Katiyar, N. K.; Kumar, R.; Parui, A.; Malviya, K. D.; Pradeep, K. G.; Singh, A. K.; Sharma, S.; Tiwary, C. S.; Biswas, K. High-entropy alloys as catalysts for the co2 and co reduction reactions: Experimental realization. *ACS Catal.* **2020,** *10*, 3658-3663.

[11] Yusenko, K. V.; Riva, S.; Carvalho, P. A.; Yusenko, M. V.; Arnaboldi, S.; Sukhikh, A. S.; Hanfland, M.; Gromilov, S. A. First hexagonal close packed high-entropy alloy with outstanding stability under extreme conditions and electrocatalytic activity for methanol oxidation. *Scripta Mater.* **2017,** *138*, 22-27.

[12] Raspolli Galletti, A. M.; Antonetti, C.; Giaiacopi, S.; Piccolo, O.; Venezia, A. M. Innovative process for the synthesis of nanostructured ruthenium catalysts and their catalytic performance. *Top. Catal.* **2009,** *52*, 1065-1069.

[13] Ertas, I. E.; Gulcan, M.; Bulut, A.; Yurderi, M.; Zahmakiran, M. Metal-organic framework (mil-101) stabilized ruthenium nanoparticles: Highly efficient catalytic material in the phenol hydrogenation. *Microporous Mesoporous Mater.* **2016,** *226*, 94-103.

[14] Wang, Y.; Yao, J.; Li, H.; Su, D.; Antonietti, M. Highly selective hydrogenation of phenol and derivatives over a pd@carbon nitride catalyst in aqueous media. *J. Am. Chem. Soc.* **2011,** *133*, 2362-2365.

[15] Scirè, S.; Minicò, S.; Crisafulli, C. Selective hydrogenation of phenol to cyclohexanone over supported pd and pd-ca catalysts: An investigation on the influence of different supports and pd precursors. *Appl. Catal., A* **2002,** *235*, 21-31.

[16] Raspolli Galletti, A. M.; Antonetti, C.; Longo, I.; Capannelli, G.; Venezia, A. M. A novel microwave assisted process for the synthesis of nanostructured ruthenium catalysts active in the hydrogenation of phenol to cyclohexanone☆. *Appl. Catal., A* **2008,** *350*, 46-52.

[17] Zhao, M.; Shi, J.; Hou, Z. Selective hydrogenation of phenol to cyclohexanone in water over pd catalysts supported on amberlyst-45. *Chin. J. Catal.* **2016,** *37*, 234-239.

[18] Ertas, I. E.; Gulcan, M.; Bulut, A.; Yurderi, M.; Zahmakiran, M. Rhodium nanoparticles stabilized by sulfonic acid functionalized metal-organic framework for the selective hydrogenation of phenol to cyclohexanone. *J. Mol. Catal. A: Chem.* **2015,** *410*, 209-220.

[19] Liu, H.; Li, Y.; Luque, R.; Jiang, H. A tuneable bifunctional water-compatible heterogeneous catalyst for the selective aqueous hydrogenation of phenols. *Adv. Synth. Catal.* **2011,** *353*, 3107-3113.

[20] Patil, R. D.; Sasson, Y. Selective transfer hydrogenation of phenol to cyclohexanone on supported palladium catalyst using potassium formate as hydrogen source under open atmosphere. *Appl. Catal., A* **2015,** *499*, 227-231.

[21] Kuklin, S.; Maximov, A.; Zolotukhina, A.; Karakhanov, E. New approach for highly selective hydrogenation of phenol to cyclohexanone: Combination of rhodium nanoparticles and cyclodextrins. *Catal. Commun.* **2016,** *73*, 63-68.

[22] Liu, H.; Jiang, T.; Han, B.; Liang, S.; Zhou, Y. Selective phenol hydrogenation to cyclohexanone over a dual supported pd–lewis acid catalyst. *Science* **2009,** *326*, 1250.

[23] Fehn, S.; Zaheer, M.; Denner, C. E.; Friedrich, M.; Kempe, R. Robustly supported rhodium nanoclusters: Synthesis and application in selective hydrogenation of lignin derived phenolic compounds. *New J. Chem.* **2016,** *40*, 9252-9256.

[24] Zhang, Z.; Ding, L.; Gu, J.; Li, Y.; Xue, N.; Peng, L.; Zhu, Y.; Ding, W. 3d charged grid induces a high performance catalyst: Ruthenium clusters enclosed in x-zeolite for hydrogenation of phenol to cyclohexanone. *Catalysis Science & Technology* **2017,** *7*, 5953-5963.

[25] Xu, G.; Guo, J.; Zhang, Y.; Fu, Y.; Chen, J.; Ma, L.; Guo, Q. Selective hydrogenation of phenol to cyclohexanone over pd-hap catalyst in aqueous media. *ChemCatChem* **2015,** *7*, 2485-2492.

[26] Yang, X.; Yu, X.; Long, L.; Wang, T.; Ma, L.; Wu, L.; Bai, Y.; Li, X.; Liao, S. Pt nanoparticles entrapped in titanate nanotubes (tnt) for phenol hydrogenation:

The confinement effect of tnt. *Chem. Commun.* **2014,** *50*, 2794.

[27] Zhang, H.; Han, A.; Okumura, K.; Zhong, L.; Li, S.; Jaenicke, S.; Chuah, G.-K. Selective hydrogenation of phenol to cyclohexanone by sio2-supported rhodium nanoparticles under mild conditions. *J. Catal.* **2018,** *364*, 354-365.

[28] Xiang, Y.; Kong, L.; Xie, P.; Xu, T.; Wang, J.; Li, X. Carbon nanotubes and activated carbons supported catalysts for phenol in situ hydrogenation: Hydrophobic/hydrophilic effect. *Ind. Eng. Chem. Res.* **2014,** *53*, 2197-2203.

[29] Li, F.; Cao, B.; Zhu, W.; Song, H.; Wang, K.; Li, C. Hydrogenation of phenol over pt/cnts: The effects of pt loading and reaction solvents. *Catalysts* **2017,** *7*, 145.